Matter

CellPress

Article

A lightweight aramid-based structural composite with ultralow thermal conductivity and high-impact force dissipation

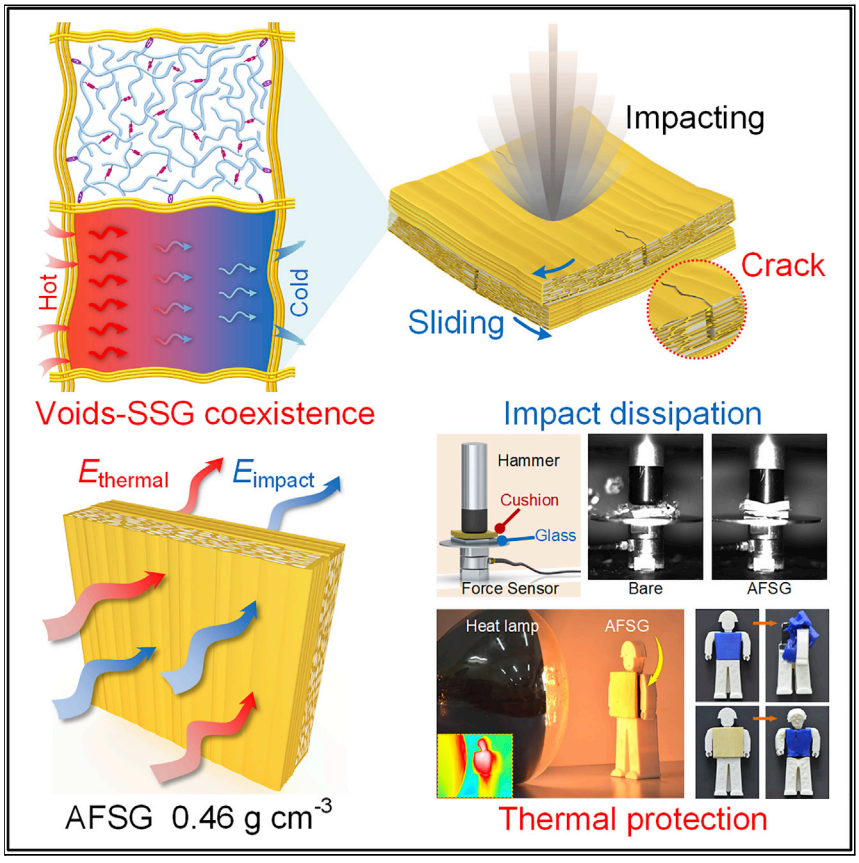

Multiple hazards including impact damage and thermal ablation usually cause abnormal operation of apparatuses. Through an ingenious infiltration and lamination strategy, commercial aramid fabrics are processed into a lightweight structural composite with ultralow thermal conductivity and high-impact force dissipation. Massive microvoids in the composite allow for exceptional thermal insulation. Structure hardening, sliding, and cracking jointly contribute to impact resistance. Such a multifunctional composite is promising to provide reliable safety protection against simultaneous impact and thermal hazards.

Demonstrate
Proof-of-concept of performance with intended application/response

Jianpeng Wu, Yu Wang, Junshuo Zhang, ..., Xiaokang He, Shouhu Xuan, Xinglong Gong

xuansh@ustc.edu.cn (S.X.)
gongxl@ustc.edu.cn (X.G.)

Highlights

Lightweight aramid-based structural material against impact and thermal hazards

Structure hardening, interlayer sliding, and intralayer cracking dissipate impact force

Microvoids and ANF scaffolds enable excellent thermal insulation and heat resistance

AFSG outperforms conventional protective materials in anti-impact and thermal insulation

Wu et al., Matter 5, 1–20
July 6, 2022
https://doi.org/10.1016/j.matt.2022.04.031

Please cite this article in press as: Wu et al., A lightweight aramid-based structural composite with ultralow thermal conductivity and high-impact force dissipation, Matter (2022), https://doi.org/10.1016/j.matt.2022.04.031

Matter

CellPress

Article

A lightweight aramid-based structural composite with ultralow thermal conductivity and high-impact force dissipation

Jianpeng Wu,[1] Yu Wang,[1] Junshuo Zhang,[1] Chunyu Zhao,[1] Ziyang Fan,[1] Quan Shu,[1] Xiaokang He,[1] Shouhu Xuan,[1,2,*] and Xinglong Gong[1,2,3,*]

SUMMARY

Material designs for safety protection are increasingly important due to ubiquitous impact damage and thermal hazard. Recent biomimetic architectures achieve extraordinary safeguards but exhibit a single-defense function, which remains a formidable challenge in mechanical-thermal-coupled protection. Herein, a lightweight composite (AFSG) with a shear stiffening gel (SSG)-filled aramid nanofiber (ANF) aerogel structure is developed through infiltration and lamination. Benefiting from the voids-SSG coexistence construction achieved by retaining massive microvoids in densified aerogel networks, AFSG exhibits ultralow thermal conductivity (0.09 W m^{-1} k^{-1}) and high-impact force dissipation. Specifically, microvoids inside AFSG greatly block heat transfer and achieve a wide insulation temperature (–120 to 300°C). SSG and the laminated-layout structure effectively attenuate 65%–79% of impact force through structure hardening, interlayer sliding, and intralayer cracking. Such a versatile, lightweight structural composite is expected to defend against simultaneous mechanical impact and heat damage as an ideal candidate for next-generation protective materials applied in transportation, military, and aerospace fields.

INTRODUCTION

Multiple hazards including mechanical impact, heat shock, and humidity erosion arising from extreme conditions usually bring troublesome problems to personnel/apparatus for normal operation, such as human injury, device malfunction, and utility degradation.[1–3] Preventing these threats, especially those caused by mechanical-thermal-coupling damage, urgently needs the construction of versatile protective materials. A common strategy lies in the compound arrangement assembly from a single-function component through simple multilayer=laminating, surface-coating, or physically blending methods to fulfill specific protection requirements in thermal management and impact resistance.[4–7] However, interface failures easily appeared in these arrangements due to the poor bonding strength among functional layers, resulting in performance deterioration over time. To provide reliable protection with rational material layout, further structure optimization in macro- or microscale based on biological models has become another available solution.[8] For example, natural nacre-mimetic "brick-mud" architectures composed of rigid plates and viscous polymers notably improved the toughness and bending stiffness of original materials through energy dissipation of interface sliding and shearing.[9] Inspired by "Bouligand" structures such as the dactyl club of mantis shrimps and the exoskeleton of coelacanths, lamellae stacked with a rotating angle could guide cracks to twist and reorient when suffering fracture, thus elevating the impact

Progress and potential

Safety protection for apparatus/personnel against mechanical and thermal damage in harsh environments requires sensible design of protective materials. Conventional safeguard architectures have difficulty defending against these complex threats. Herein, through an ingenious infiltration and lamination approach, commercial aramid fabrics are processed into a lightweight laminated composite with void-filler coexistence structure. This composite is proven to have an ultralow thermal conductivity owing to the presence of microvoids that weaken heat conduction and convection. It can also attenuate a wide range of impact forces by structural hardening, along with structural failures by sliding and cracking. Such a perfect coordination between thermal insulation and impact dissipation innovates multifunctional defense design, allowing this aramid-based composite to be a candidate for next-generation lightweight protective materials for applications in transportation, military, and aerospace fields.

Please cite this article in press as: Wu et al., A lightweight aramid-based structural composite with ultralow thermal conductivity and high-impact force dissipation, Matter (2022), https://doi.org/10.1016/j.matt.2022.04.031

resistance of plywood materials.[10,11] Mimicking the hollow tubular polar bear fur, microporous networks (e.g., aerogels and foams) achieved exceptional heat insulation capacity that was orders of magnitude higher than original solid forms.[12–14] These unique biomimetic mechanisms allow functional materials to realize optimal protection efficiency yet feature lightweight and portable attributes.[15–17] Nevertheless, since mechanical impacts occurring in harsh environments are often accompanied b y thermal damage,[18,19] the traditional single-defense construction is impotent to resist these coupled threats. More comprehensive consideration should be given in the design of protective materials to achieve a wisely reconciled tradeoff between thermal protection and impact absorption.

Generally, the isolation of heat diffusion in porous networks mainly depends on the pore microstructures, because it is easier for high porosity along with small pore size to weaken thermal conduction and air convection compared with loose structures.[20] For example, a double-pane ceramic aerogel showed lower thermal conductivity at high density (24–20 mW m^{-1} k^{-1} versus 0.1–10 mg cm^{-3}), owing to the decreased pore size and pane distance.[13] Whereas the mechanical strengths of solid constituents (e.g., scaffolds and internal fillers) largely determine impact resistance behavior, as they provide support for entire networks to avoid catastrophic failure under external loading,[21] such as an epoxy-infiltrated inverse nacre structure significantly enhanced the facture toughness of original graphene networks.[22] Previously, most endeavors focused on unilateral utility enhancement, like densification engineering for microvoid elimination or supercritical drying to improve specific surface area,[23–26] without taking into account the synergistic effect between porous networks and solid constituents. Therefore, rationally modulating these two factors in material preparations is very necessary to realize mutual coordination in impact and thermal protections.

Aramid nanofibers (ANF), known as one-dimensional (1D) nanoscale building blocks owing to their excellent thermal and chemical stabilities,[27,28] can be processed into porous aerogel structures with ultralow thermal conductivity. Recently reported 1D threads and three-dimensional (3D) monoliths derived from ANF aerogels have been demonstrated to show comparable heat insulation capacity to air and manifest potential thermal protection utility at extreme temperatures.[20,29] However, the low compressive strength of porous networks in ANF aerogels severely limits their further application in load-carrying engineering frames.[29] Shear stiffening gel (SSG) is a kind of viscoelastic polymer that possesses unique rate-dependent mechanical behavior, as its storage modulus can increase rapidly with shear rate.[30] This stiffening effect allows it to transfer from a viscous flow phase to an elastic state in response to high strain rate loading and generate structure-hardening against mechanical impact.[5] To this end, the SSG can be exploited to reinforce the unsatisfactory compression property of ANF aerogels.

In this work, we devise a pore-remaining filling aerogel structure jointly composed of cellular scaffolds, filler, and voids (Figure 1B). Specifically, ANF aerogels with aligned scaffolds prepared by unidirectional freeze-casting are chosen to be the porous hierarchical networks.[31] SSG serves as a load-bearing constituent to fill the scaffolds while retaining randomly distributed voids. The voids-SSG coexistence networks are finally orthogonally laminated into a lightweight structural composite (AFSG, namely ANF aerogel infiltrated with SSG, 0.46 g cm^{-3}), which exhibits simultaneously high impact force dissipation and ultralow thermal conductivity beyond those of traditional cushioning materials. Dual-protection mechanisms can be drawn from the resultant compound construction. First, filled SSG facilitates stress

[1]CAS Key Laboratory of Mechanical Behavior and Design of Materials, Department of Modern Mechanics, University of Science and Technology of China (USTC), Hefei, Anhui 230027, PR China

[2]State Key Laboratory of Fire Science, University of Science and Technology of China (USTC), 96 Jinzhai Road, Hefei, Anhui 230026, PR China

[3]Lead contact

*Correspondence: xuansh@ustc.edu.cn (S.X.), gongxl@ustc.edu.cn (X.G.)

https://doi.org/10.1016/j.matt.2022.04.031

Please cite this article in press as: Wu et al., A lightweight aramid-based structural composite with ultralow thermal conductivity and high-impact force dissipation, Matter (2022), https://doi.org/10.1016/j.matt.2022.04.031

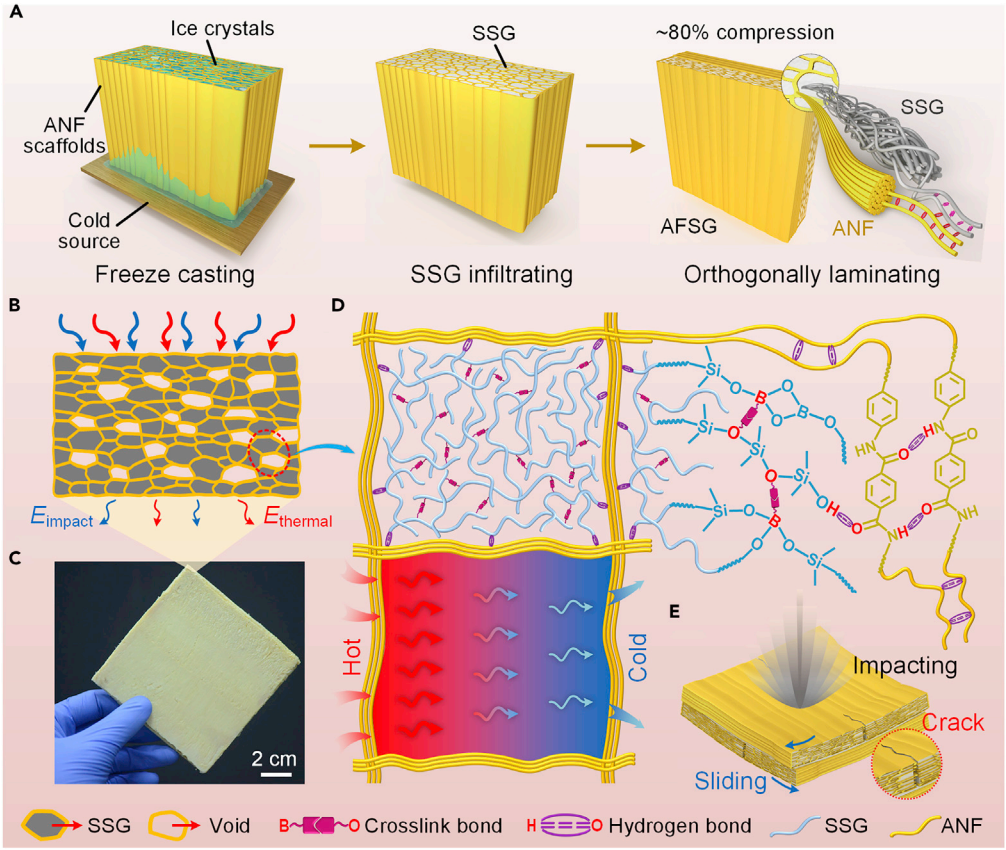

Figure 1. Preparation process and protection mechanism against thermal and impact damage of AFSG

(A) Schematic showing the specific preparation process of AFSG.

(B) Cross-sectional schematic of AFSG illustrating the voids-SSG coexistence structure that effectively dissipated inward E_{impact} and $E_{thermal}$.

(C) Photograph of AFSG with surface area of 10 × 10 cm^2.

(D) Representative voids-SSG structure and corresponding SSG and ANF molecular chains. The twisted arrows denote thermal conduction paths in the void part.

(E) Schematic image for the intralayer cracks and interlayer sliding occurring at impact process.

enhancement of AFSG to resist high strain rate compression. The laminated layout bonded by SSG further guides the manner of failure of interlayer sliding and intralayer crack to dissipate excessive impact energy, thus ensuring a broad defense range to mechanical damage. Second, massive microscale voids in AFSG block internal heat transfer along the lamination direction, while stable ANF scaffolds hinder external thermal ablation, enabling a wide insulation temperature (−120 to 300°C) as well as robust heat resistance (negligible morphological change after heating with 300°C for 30 min). Because of this extraordinary performance, AFSG is expected to possess broad application potential in next-generation lightweight, multifunctional, protective materials.

RESULTS AND DISCUSSION

Preparation of AFSG

The preparation of AFSG mainly involved unidirectional freeze-casting, SSG infiltrating into ANF scaffolds, and orthogonal laminating (Figure 1A). First, a dark red ANF dispersion was prepared by deprotonation of aramid fabrics in dimethyl sulfoxide (DMSO) solvent. Then, it was transferred into deionized water for gelation (Figure S1A, left), in which DMSO was removed thoroughly, accompanied by the

Please cite this article in press as: Wu et al., A lightweight aramid-based structural composite with ultralow thermal conductivity and high-impact force dissipation, Matter (2022), https://doi.org/10.1016/j.matt.2022.04.031

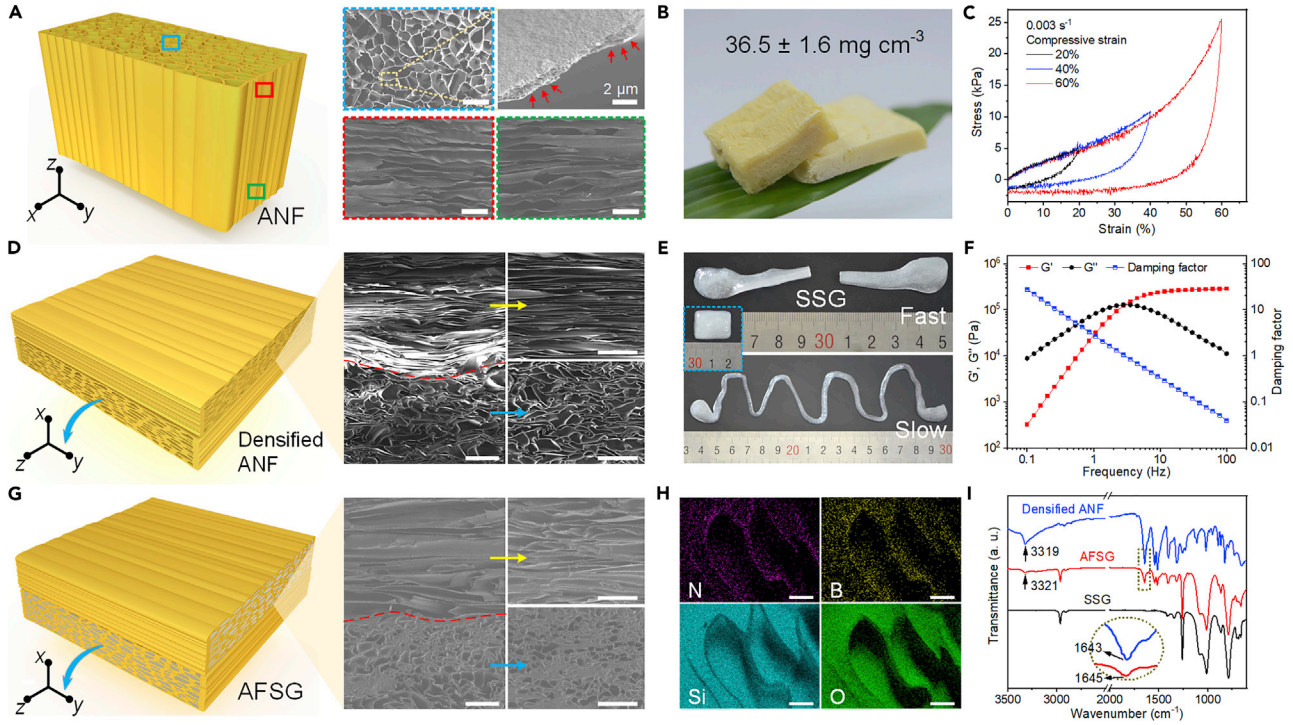

Figure 2. Morphology characterizations of ANF aerogel, densified ANF block, SSG, and AFSG

(A) Schematic diagram and SEM images of ANF aerogel. Scale bars, 500 μm. The red arrows in the top right denote the edge of multilayer nanoflakes.

(B) Photograph of lightweight ANF aerogels.

(C) Compressive stress-strain curves of ANF aerogel under strain of 20%–60% and rate of 0.003 s^{-1}.

(D) Schematic diagram and cross-sectional SEM images of densified ANF block. Scale bars, 300 μm. The red dotted line denotes the laminated interface.

(E) Optical images illustrating the rate-dependent viscoelastic behavior of SSG (see also Video S1).

(F) Dependence of storage modulus (G′), loss modulus (G″), and damping factor of SSG on oscillating shear frequency under strain of 0.1%.

(G) Schematic diagram and cross-sectional SEM images of AFSG. Scale bars, 300 μm. The red dotted line denotes the laminated interface.

(H) Energy-dispersive spectroscopy (EDS) maps showing the detected elements (nitrogen, boron, silicon, and oxygen) of AFSG. Scale bars, 25 μm. See also Figure S6.

(I) FTIR spectra of AFSG, SSG, and densified ANF block.

formation of intermolecular hydrogen bonds among the ANF.[20] The hydrogel was further contacted with a cold source (copper plate, −70°C) cooled with liquid nitrogen (Figure S1A, middle). Driven by the temperature gradient between liquid nitrogen and ANF hydrogel, a large number of ice crystals grew perpendicular to the cold source and occupied the internal space of homogenous hydrogel, squeezing the ANF into anisotropic scaffolds (Figure 1A, left). After freeze-drying at −50°C and 10 Pa for 48 h, the ice crystals gradually sublimated from the hierarchical porous networks of the ANF aerogel (Figure 2A). Then, the SSG-ethanol dispersion was infiltrated into the oriented scaffolds to thoroughly fill the microscale pores (Figure 1A, middle, and Figure S1C, left), where the self-supporting ANF scaffolds provided effective restraint for internal filler. After compounding with SSG, two pieces of the same ANF aerogel were orthogonally laminated at 80°C to densify the porous networks and remove residual ethanol (Figure 1A, right, and Figure S1C, right). The resultant AFSG had a pale yellow appearance (Figure 1C) as did the laminated cross-section (Figure 2G). It is worth noting that not all pores were filled, as part of SSG microblocks were squeezed out with the solvent (ethanol) during the lamination process, thus leading to the simultaneous existence of SSG cores and voids in the AFSG (Figure S3F).

Please cite this article in press as: Wu et al., A lightweight aramid-based structural composite with ultralow thermal conductivity and high-impact force dissipation, Matter (2022), https://doi.org/10.1016/j.matt.2022.04.031

Such a unique voids-SSG coexistence structure was able to effectively dissipate both the mechanical impact energy (E_{impact}) and the thermal energy ($E_{thermal}$) (Figure 1B). Specifically, the typical voids-SSG structure in Figure 1D contained massive flexible SSG molecular chains, whose hydroxyl groups formed hydrogen bonds with carbonyl groups of rigid ANF chains, achieving strong adhesion between ANF scaffolds and SSG cores. More importantly, the abundant dynamic crosslinking bonds (B-O bonds) in SSG could resist high strain rate loading and connect the entangled SSG chains into a robust web,[30] which enabled the AFSG to generate macroscopic structure hardening when subjected to impact energy. Besides the stiffening effect of SSG, oriented ANF scaffolds and orthogonal lamination arrangement tended to generate intralayer cracks as well as interlayer sliding during the impact process (Figure 1E).[21] These failure fashions were able to absorb excessive impact energy and provide further protection against mechanical damage. On the other hand, the voids randomly distributed in AFSG played a vital role in thermal insulation (Figure 1B). As shown in the bottom half of Figure 1D, the microsize space enclosed by ANF scaffolds could effectively hinder air flow and eliminate heat convection along the lamination direction. Heat conduction input from surrounding solid parts was greatly weakened as well by the low thermal conductivity air (0.023 W m^{-1} k^{-1}) in the void parts,[32] thus achieving a large temperature difference between the adjacent ANF scaffolds. Such a sensible design of voids-SSG structure will be further discussed below.

Morphological characterization of AFSG

Harnessing unidirectional freeze-casting, ANF aerogel was processed into an anisotropic and porous microstructure with highly oriented multi-lamellae (Figure 2A). Figures 2B, S2A, and S2B show that the prepared ANF aerogel had a yellow appearance and an ultralow density of 36 mg cm^{-3}. As shown in Figure 2A, the top view in the blue frame validated the porous honeycomb networks welded by multiple ANF sheets that mainly formed rectangular and pentagonal pore shapes with equivalent diameters of 100–300 μm (Figure S2C). The enlarged image of top view (Figure 2A, right) reveals that the single ANF wall was overlaid by multilayer nanoflakes (red arrows represent the edge of nanoflakes), which acted as a basic skeleton to provide self-supporting and load-bearing capacities for whole aerogel. The long-range aligned ANF sheets (Figure 2A, red and green frames) along the ice crystals' growth direction kept similar interlayer spacing in the top and bottom of material of up to 3 cm (Figure S2B), reflecting the feasibility of large-scale hierarchical microstructure design through unidirectional freeze-casting. The quasi-static compression property of ANF aerogel was investigated (Figure 2C). It had similar loading trajectories from 20% to 60% compressive strain. The low initial modulus (22.3 kPa) and increased hysteresis area with strain stemmed from the elastoplastic scaffolds and large pores of ANF aerogel that required enough deformation to resist compressive force. Two pieces of the same aerogel were further orthogonally laminated at 80°C. After the densification process, ANF scaffolds underwent severe collapse accompanied by pore wall distortion and stacking (Figure S3C) owing to the low compressive strength of the aerogel. The resultant densified ANF block exhibited a laminating structure as well as a compact porous network (Figure 2D) containing massive voids (Figure S3C).

Figure S4A exhibits the smooth surface of homogeneous viscoelastic SSG. Because of the intrinsic cold-flow feature, the SSG block rapidly collapsed into a flat shape over time without external loading (Figure S7A, right).[30] Typically, its thickness decreased by 63% after 210 min (Figure S7B). A creep test further validated its viscous characteristic (Figure S4B). The shear strains of SSG slowly rose under constant loading stresses but hardly changed after the stresses were removed at 10 s.

Please cite this article in press as: Wu et al., A lightweight aramid-based structural composite with ultralow thermal conductivity and high-impact force dissipation, Matter (2022), https://doi.org/10.1016/j.matt.2022.04.031

Figure 2E and Video S1 show two deformation modes of a cylindrical SSG that were stretched manually with different intensities. Apparently, a mild speed could extend it to tens of times the original length without breaking, whereas a high stretching rate led to a brittle fracture due to the dynamic force impedance of B-O crosslinks among SSG molecular chains.[33] The rheological characteristic of SSG was further investigated (Figure 2F). A key parameter, storage modulus (G′), the ability to store elastic energy, improved significantly, from 323 to 283 kPa as shear frequency increased from 0.1 to 100 Hz, suggesting a prominent shear stiffening effect. Meanwhile, at the initial shearing stage, the damping factor of SSG had a maximum value of 27 owing to the viscous feature under low strain rate, which meant a high energy-dissipation capacity of SSG. With increasing shear frequency, the internal friction among SSG molecular chains, as well as movement hindrance caused by B-O crosslinks, increased more noticeably.[33] This stiffening effect led to the phase transition of SSG from viscous flow to elastomeric state along with decreased damping factor.

Derived from the unique viscous characteristic of SSG, AFSG could be prepared though infiltrating SSG into porous ANF aerogel networks. After two pieces of SSG-infiltrated ANF aerogel were orthogonally laminated, the honeycomb pore walls collapsed and became distorted, accompanied by SSG microblock condensation, forming a compact voids-SSG coexistence structure inside the AFSG (Figure 2G, right, and Figure S3F). In addition, the aligned sheets along the freezing direction got closer to each other and thicker than that of the ANF aerogel after absorbing SSG (Figure S5). A cross-sectional image revealed a pair of orthogonal ANF scaffolds, where SSG functioned as a glue to tightly bind the overlaid interface (red dotted line in Figure 2G). EDS maps from the enlarged view of AFSG (Figure S6) verified the even distribution of N, B, Si, and O elements (Figure 2H). Benefiting from the self-supporting ANF scaffolds, AFSG effectively confined SSG in the pore walls and achieved long-term shape stability under the natural state (Figure S7A, left) as its thickness remained unchanged throughout the whole process (Figure S7B). Furthermore, the introduction of SSG in turn endowed AFSG with exceptional water resistance performance, as verified in Figure S8.

The comparison of FTIR spectra among AFSG, densified ANF block, and SSG is shown in Figure 2I. Typical characteristic peaks of ANF, such as the stretching vibration peaks originated from N-H (3,319 cm^{-1}), C=O (1,643 cm^{-1}), and C=C (1,511 cm^{-1}) groups, were detected in AFSG.[34] After the introduction of SSG, AFSG exhibited peaks located at 1,342 cm^{-1}, 1,008 cm^{-1}, and 862 cm^{-1}, which were ascribed to the stretching vibrations of B-O, Si-O-Si, and Si-O-B groups, respectively.[33] In addition, the original N-H (3,319 cm^{-1}) and C=O (1,643 cm^{-1}) groups existing in the densified ANF block shifted to a higher wave number in AFSG. The slight change of peak positions was probably due to the formation of a small number of intermolecular hydrogen bonds between SSG and ANF chains (Figure 1D).

Rate-dependent compressive behavior of AFSG

The low strain rate compression property of AFSG was investigated systematically. Figure 3A reveals that all the loading-unloading curves were nearly consistent from 0.003 to 0.1 s^{-1}, indicating a weak rate-dependent mechanical property of densified ANF block. Nevertheless, the scaffolds were proven to have excellent resilience, since 78% of maximum stress was retained even after 5,000 cycles of compression (Figure S9), which was conducive to resisting fatigue failure. Generally, macroscopic mechanical properties of structural materials largely depend on their

Please cite this article in press as: Wu et al., A lightweight aramid-based structural composite with ultralow thermal conductivity and high-impact force dissipation, Matter (2022), https://doi.org/10.1016/j.matt.2022.04.031

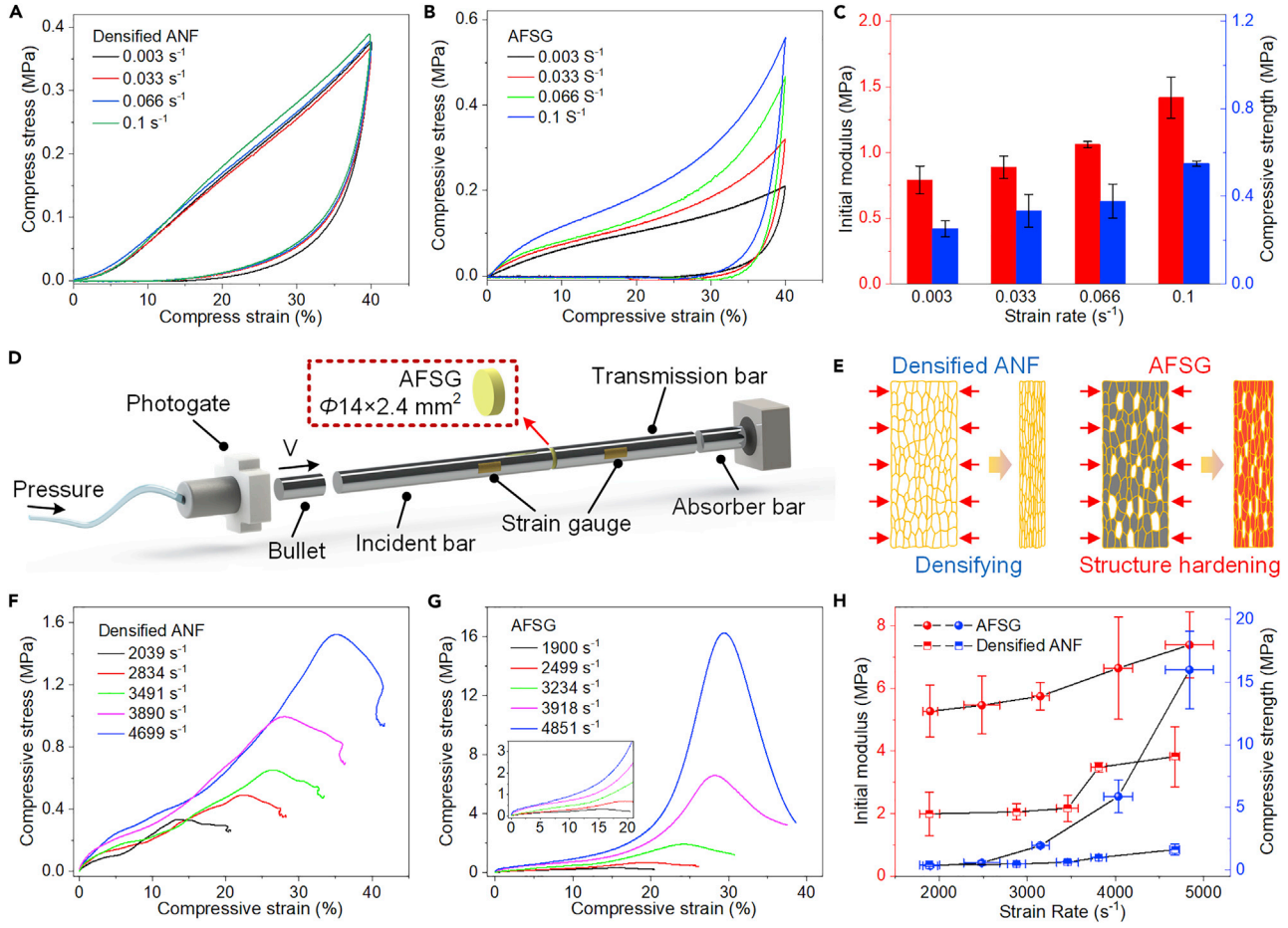

Figure 3. Rate-dependent compressive property of AFSG

(A and B) Compressive stress-strain curves of (A) densified ANF block and (B) AFSG under low strain rate loading.

(C) Dependence of initial modulus and compressive strength on strain rate of AFSG. Data are represented as mean ± SEM.

(D) Schematic illustrating the SHPB system. It mainly consists of bullet, incident bar, and transmission bar.

(E) Schematic showing the scaffold densifying and structure hardening occurring to densified ANF block and AFSG, respectively, at high strain rate compression. Black to red transition in AFSG represents the stiffening effect of internal SSG.

(F and G) Compressive stress-strain curves of (F) densified ANF block and (G) AFSG at different strain rates. Note that all stresses and strains measured by SHPB represent true stresses and true strains.

(H) Dependence of initial modulus and compressive strength on strain rate. Data are represented as mean ± SEM. Note that the densities of AFSG and densified ANF block were 0.46 g and 0.16 g cm^{-3}, respectively. See also Figure 5E.

microstructures. For example, higher strength and toughness could be achieved by constructing material into oriented arrangement.[35] A sandwich structure possessed better impact resistance than a hollow structure.[36] Herein, by virtue of shear stiffening gel-assisted hierarchical porous networks, AFSG exhibited obvious strain hardening under high loading rate (Figure 3B). Both the initial modulus and the maximum stress improved significantly, from 0.8 MPa to 251 kPa at 0.003 s^{-1} to 1.41 MPa and 549 kPa at 0.1 s^{-1} (Figure 3C). It is a fact that the internal SSG cores supported entire ANF scaffolds and avoided catastrophic collapse due to their dynamic force impendence effect. Furthermore, the energy dissipation density of AFSG, namely the area of stress-strain hysteresis curve (Figure S10), was also gradually enhanced, from 4.3 to 7.3 MJ m^{-3} when the strain rate increased from 0.003 to 0.1 s^{-1}, reflecting its potential application in impact resistance and energy absorption.

Please cite this article in press as: Wu et al., A lightweight aramid-based structural composite with ultralow thermal conductivity and high-impact force dissipation, Matter (2022), https://doi.org/10.1016/j.matt.2022.04.031

In order to further study the high strain rate compressive property, a spilt Hopkinson pressure bar (SHPB) system, which mainly consisted of a bullet, incident bar, and transmission bar (Figure 3D), was used to realize high-speed loading. As shown in Figure 3G, AFSG exhibited a strong rate-dependent behavior. The initial modulus and compressive strength increased noticeably from 5.27 and 0.32 MPa at 1,900 s^{-1} to 7.39 and 16.24 MPa at 4,851 s^{-1}. Within the initial loading phase, AFSG underwent elastic deformation with low loading slopes due to the preliminary shrinkage of internal voids. A further increase of compressive strain triggered the structure hardening of dense AFSG (Figure 3E, right), leading to abrupt stress enhancement under the 20%–30% stage. Especially, when the strain rates were kept at 3,918 and 4,851 s^{-1}, the maximum stress reached 6.57 and 16.24 MPa, respectively. This could be ascribed to the significant stiffening effect of SSG under high strain rate loading (Figure S11), which was produced by the friction of entangled SSG molecular chains and the dynamic deformation hindrance of B-O cross-linking bonds (Figure 1D). As a comparison, the densified ANF block maintained massive voids surrounded by distorted ANF sheets (Figure 2D). These voids were easily compacted during compression (Figure 3E, left) and resulted in approximate linear deformation from 2,039 to 4,699 s^{-1} (Figure 3F). The variations of modulus and strength to strain rate (Figure 3H) also revealed the slight stress enhancement and poor compression resistance of the densified ANF block. In contrast, the significant rate dependence of strength and initial modulus (Figure 3H) suggested that AFSG was able to absorb more mechanical energy under high-speed impact compared with the densified ANF block.

Anti-impact performance of AFSG

Considering that the compressive stress enhancement occurred at a high strain rate, it was speculated that AFSG could resist mechanical impact damage. Herein, a low-velocity impact experiment was implemented to explore the anti-impact property, in which the drop hammer freely fell from a specific height (*h*) to the specimen in a non-penetrating manner (Figure 4A). As shown in Figures 4D–4G, the reference groups exhibited dramatically enhanced impact force (2–6.34 kN) along with a short buffer time (less than 1 ms) as the height increased from 10 to 70 cm, reflecting an intensive damage hazard induced by impact energy. In contrast, AFSG largely attenuated the impact forces and prolonged the buffer times of the reference groups. Although AFSG had slightly higher force peaks than the densified ANF block at low drop heights (0.44 versus 0.24 kN at 10 cm, 1.22 versus 1.15 kN at 30 cm), the enhanced structure hardening generated by SSG at high drop velocity facilitated the rapid improvement of impact resistance of AFSG, thus enabling superior force dissipation at high drop heights (1.66 versus 2.88 kN at 50 cm, 2.13 versus 4.36 kN at 70 cm). To further illustrate the anti-impact utility of SSG, a finite-element model (FEM, Figure 4B) was established by reconstructing the voids-SSG coexistence structure of AFSG according to the cross-sectional SEM image in Figure S12 (corresponding details are in Note S1). Another FEM of pure ANF scaffolds extracted from the voids-SSG structure was regarded as a control (Figure S13A, left). Both of them suffered an impact action on the top surface, with an initial velocity (v_0) of 0.4 m s^{-1} (Figures 4C and S13A, right). As shown in Figure S13B, the normalized contact force between voids-SSG FEM and ground showed lower peak as well as longer duration time than that of ANF scaffolds FEM, indicating a crucial role of SSG in the impact force dissipation of AFSG.

By estimating the attenuation percentage of maximum impact force (F_{max}) relative to the reference groups, it could be known that AFSG exhibited a high attenuation coefficient up to 79% and robust impact tolerance against 6.34 kN arising from 70 cm

Please cite this article in press as: Wu et al., A lightweight aramid-based structural composite with ultralow thermal conductivity and high-impact force dissipation, Matter (2022), https://doi.org/10.1016/j.matt.2022.04.031

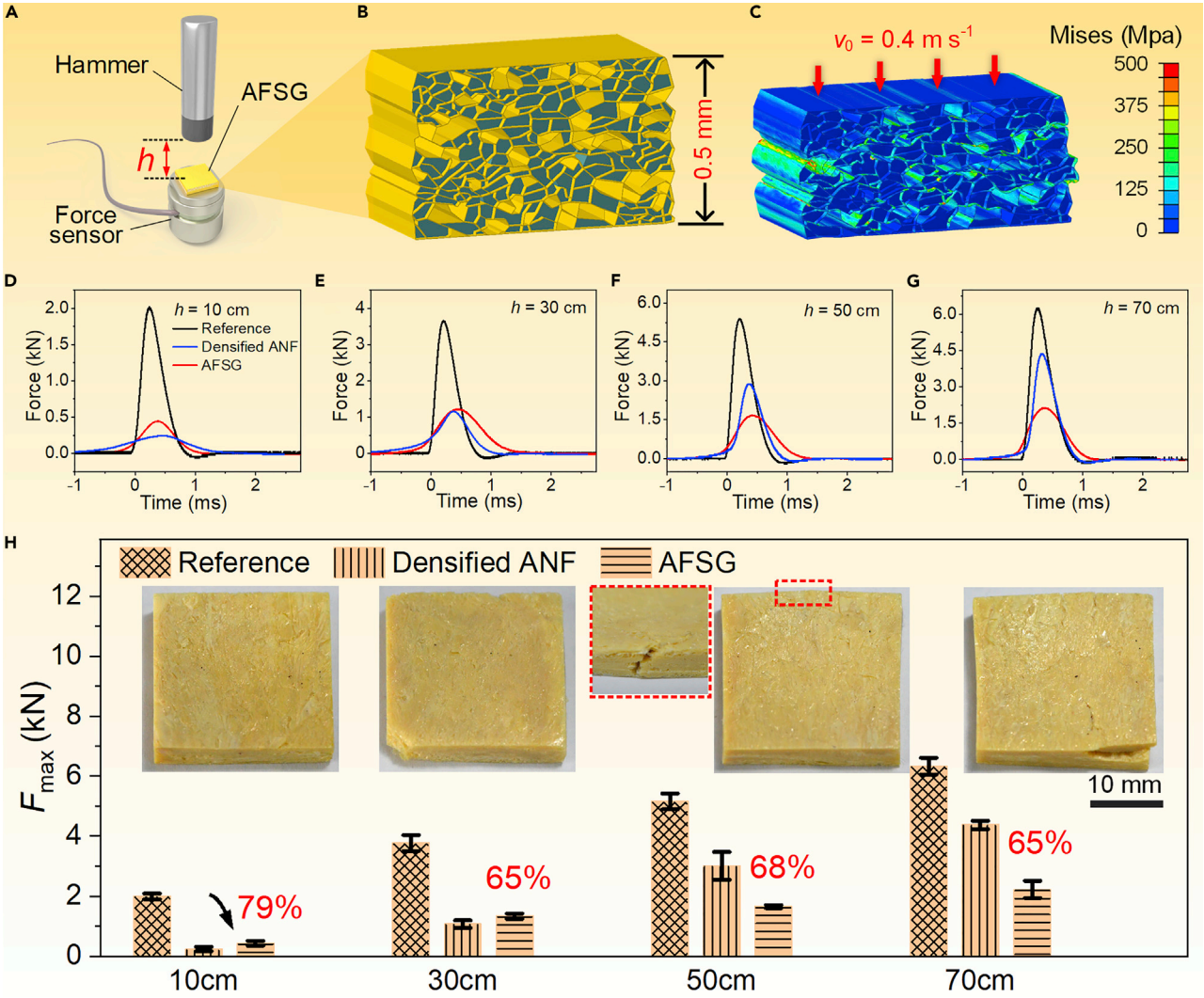

Figure 4. Impact resistance performance of AFSG

(A) Schematic of drop hammer impact test system.

(B) Finite element model reconstructing the voids-SSG coexistence structure of AFSG. See also Figure S12.

(C) Corresponding von Mises stress distribution of FEM model under maximum impact deformation with an initial velocity of 0.4 m s^{-1}.

(D–G) Force-time curves of AFSG and densified ANF block during impact process from heights of (D) 10 cm, (E) 30 cm, (F) 50 cm, and (G) 70 cm, respectively. Note that the force signals of reference condition represent direct impact of hammer toward force sensor.

(H) Corresponding F_{max} of AFSG and densified ANF block estimated from (D–G). Data are represented as mean ± SEM. (Insets represent surface morphologies of AFSG after impact. Red text represents percentage of force attenuation.) Note that the densities of AFSG and densified ANF block were 0.46 g and 0.16 g cm^{-3}, respectively. See also Figure 5E.

(Figure 4H). In addition, the photographs of AFSG after the test (insets in Figure 4H) revealed an intact appearance at 10–30 cm owing to the recoverable elastic deformation of ANF scaffolds under low impact height. When the height was further increased to 50–70 cm, AFSG showed mild central depression accompanied by intralayer crack and interlayer sliding, but no extensive rupture appeared. This failure fashion effectively absorbed a large amount of impact energy, which benefited from the orthogonally laminating structure (see detailed explanation in Note S3). In contrast, the absence of SSG led to poor compression resistance of the densified ANF block (Figures 3F and 3H), in which serious central deformation and interlayer delamination appeared at 50–70 cm (Figure S17). The poor damage endurance

Please cite this article in press as: Wu et al., A lightweight aramid-based structural composite with ultralow thermal conductivity and high-impact force dissipation, Matter (2022), https://doi.org/10.1016/j.matt.2022.04.031

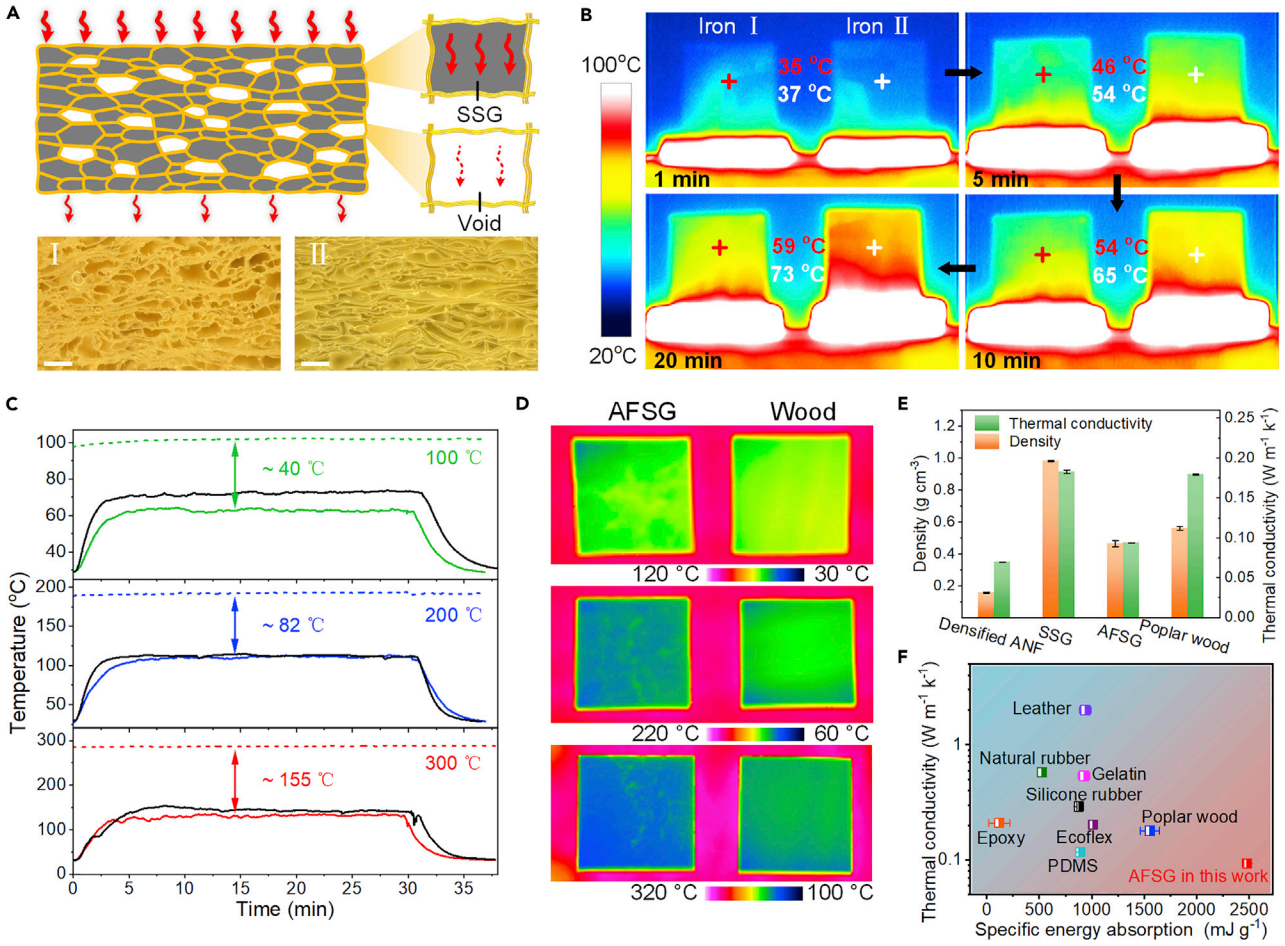

Figure 5. Thermal insulation behavior of AFSG

(A) Schematic illustrating the voids-SSG coexistence structure of AFSG for thermal insulation (top). The red arrows in voids and SSG denote thermal transfer process. Cross-sectional optical micro-images of AFSG (I) and highly filled AFSG (II), respectively (bottom; scale bars, 200 μm).

(B) Infrared images showing the temperature distributions of iron blocks placed on AFSG (I) and highly filled AFSG (II). See also the schematic in Figure S18.

(C) Temperature changes of AFSG (colored lines) and poplar wood (black lines) at stage temperature of 100°C, 200°C, and 300°C, respectively (dotted lines).

(D) Corresponding infrared images of (C) at 30 min. The area of all specimens was 25 × 25 mm^2 with a thickness of 5 mm.

(E) Thermal conductivities and densities of densified ANF block, SSG, AFSG, and poplar wood, respectively.

(F) Comparison in thermal conductivity and specific energy absorption of AFSG with conventional buffer materials (Epoxy, polydimethylsiloxane (PDMS), Eco-flex, poplar wood, silicone rubber, gelatin, natural rubber, and leather. See also Figure S22 and Table S2).

In (E and F), data are represented as mean ± SEM.

highlighted an indispensable role for SSG in assisting ANF scaffolds to resist high impact energy.

Thermal insulation property of AFSG

Exceptional thermal insulation behavior is desirable for structural materials to ensure normal operation of devices at extreme temperatures and to reduce energy loss in intensive heat diffusion. Generally, high-porosity architecture possesses lower thermal conductivity than solid structures owing to the limited thermal conduction mediums composed of pore walls and internal gaps.[32] As shown in Figure 5A, microsize voids randomly distributing in AFSG (Figure 5AI) were expected to convert the solid conduction in SSG cores to weak gas conduction in voids. Herein, a highly filled

AFSG (Figures 5AII and S18A) with a density of 0.60 g cm^{-3} (Table S1) was fabricated by repeatedly infiltrating SSG into ANF aerogel networks to eliminate residual voids. The thermal resistance performance of the highly filled AFSG was compared with AFSG in this work. Briefly, two iron blocks with the same size of 25 × 25 × 5 mm^3 were placed on surfaces above AFSGs and heated by a stable hot source (250°C) (Figure S18B). Due to the numerous thermal conduction channels given by SSG cores in highly filled AFSG, iron block II had a fast heat transfer rate along the vertical direction, whose central temperature reached 73°C rapidly within 20 min (Figure 5B), whereas the voids existing in AFSG effectively hindered heat spread toward iron block I and led to an increased temperature difference over time with iron block II, which reflected a better heat-resistant property of AFSG.

Derived from the unique voids-SSG coexistence architecture (Figure 5A), AFSG was proven to have superior thermal insulation capacity to that of traditional woods (such as poplar wood). Specifically, AFSG and poplar wood were placed on a hot plate with constant temperature ranging from 100°C to 300°C. The variations in temperature of the specimens and hot plate were measured simultaneously using thermocouples. As shown in Figure 5C, the surface temperatures of all specimens rose to an equilibrium state within 5–10 min and then fluctuated slightly. Compared with poplar wood, AFSG maintained a higher temperature difference (ΔT) with the hot plate after heating for 30 min and reached a maximum value of 155°C under the extreme high temperature of 300°C. Corresponding thermal images recorded by infrared camera at 30 min also revealed that the temperatures on the surface of AFSG were lower (Figure 5D). Moreover, even with contact with a cold plate at an initial −120°C, AFSG maintained ΔT of 30°C for at least 40 min (Figure S19). The superwide thermal resistance range (−120 to 300°C) as well as long-term insulation stability of AFSG (Figure S20) is quite rare among existing structural materials, allowing for broad application in harsh conditions such as the military field and aerospace. We further determined the thermal conductivities of AFSG and poplar wood (Figure 5E). The results suggested that AFSG had an ultralow thermal conductivity of 0.09 W m^{-1} k^{-1}, which was only half that of the poplar wood (0.18 W m^{-1} k^{-1}). This could be attributed to the synergistic effect brought by low thermal conductivities of raw materials (densified ANF block and SSG; Figure 5E) and widely distributed voids inside the AFSG. Besides, the massive voids also achieved a lightweight characteristic (0.46 g cm^{-3}) of AFSG and there remained more air gaps for heat isolation compared with the poplar wood. As shown in Figure S21, the thermal performance of AFSG was also compared with many other materials. The thermal conductivity of AFSG was similar to that of porous aerogels (e.g., Mxene-ANF aerogel, silica aerogel) and lower than that of some commercial thermal insulators (e.g., asbestos, PVC tube). The results above indicated that AFSG could provide reliable thermal protection for equipment/personnel at extreme temperatures. Furthermore, it is worth noting that our AFSG gained both low thermal conductivity and high impact energy absorption, which are usually mutually exclusive in conventional engineering materials (Figures 5F and S22 and Table S2), wherein the energy absorption behaviors of all samples were estimated by calculating the kinetic energy difference of the drop hammer during impact tests (corresponding details can be found in Note S2). Such a perfect coordination of heat insulation and impact resistance in AFSG benefited from the sensible design of voids-SSG coexistence architecture inside hierarchical ANF networks, which further enabled a great potential to defend against multi-physical damage in extreme environments.

Demonstrations of AFSG in anti-impact and thermal protection

Extraordinary energy absorption and force attenuation capacities endowed AFSG with actual anti-impact utility (Figure 6A). As shown in Figures 6B–6D and Video

Please cite this article in press as: Wu et al., A lightweight aramid-based structural composite with ultralow thermal conductivity and high-impact force dissipation, Matter (2022), https://doi.org/10.1016/j.matt.2022.04.031

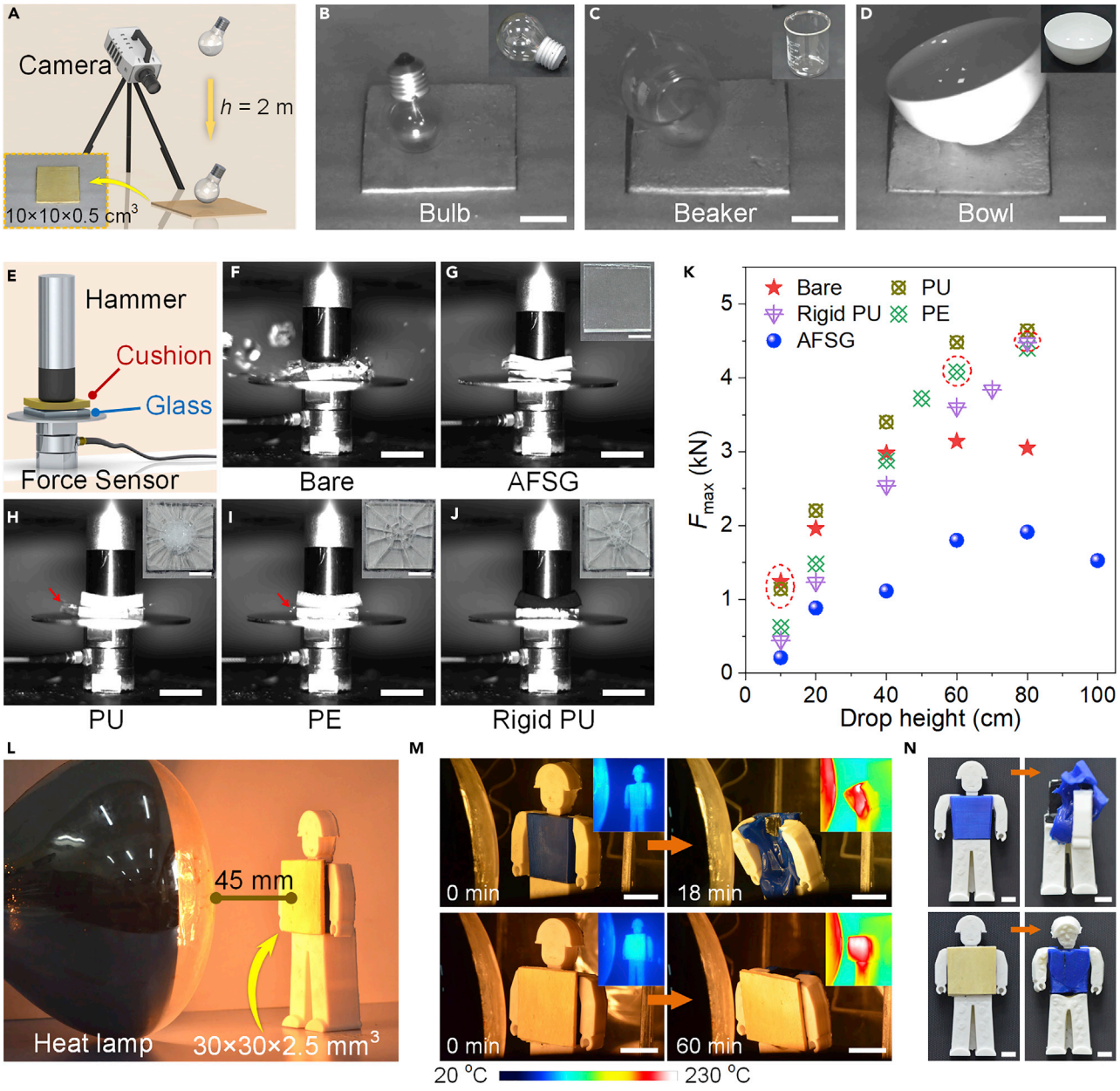

Figure 6. Demonstrations of impact resistance and thermal protection

(A) Schematic of the freely dropping process recorded by high-speed camera.

(B–D) Snapshots of (B) bulb, (C) beaker, and (D) bowl hitting AFSG that freely dropped from 2 m height (see also Video S2). Scale bars, 30 mm.

(E) Schematic illustrating the impact protection behavior of AFSG.

(F–J) Snapshots of impact moment of glasses protected with (F) nothing, (G) AFSG, (H) PU foam (0.025 g cm^{-3}), (I) PE foam (0.040 g cm^{-3}), and (J) rigid PU foam (0.136 g cm^{-3}), respectively (see also Video S3). Scale bars, 20 mm. (Red arrows indicate glass shards. Insets represent the morphologies of glasses after impact. Scale bars, 10 mm).

(K) Corresponding F_{max} of (F–J) from 10 to 100 cm height. (Red circles represent the initial height of glass breakage).

(L) Thermal protection of toy man under the baking of a heat lamp. The body part of this toy was attached with AFSG.

(M) Optical images of thermal damage to toy man with and without the protection of AFSG. Scale bars, 20 mm (insets represent corresponding infrared images).

(N) Comparison of morphological changes of toy men before and after baking. Scale bars, 10 mm.

Please cite this article in press as: Wu et al., A lightweight aramid-based structural composite with ultralow thermal conductivity and high-impact force dissipation, Matter (2022), https://doi.org/10.1016/j.matt.2022.04.031

S2, glass bulb, beaker, and ceramic bowl, respectively, free-fell from a 2-m height onto the surface of AFSG (10 × 10 × 0.5 cm^3). The drop process recorded by high-speed camera revealed good preservation of these objects at the contact moment with AFSG, which was in sharp contrast to the fatal devastation caused by falling directly onto the floor (Figure S23). The outstanding cushioning effect indicated the thoroughness of AFSG in damage protection for common fragile products. In order to visualize the impact resistance of AFSG more intuitively, traditional buffer foams (polyurethane [PU] foam, polyethylene [PE] foam, and rigid PU foam), the most representative commercial cushioning materials for product protection and transportation, were selected as comparisons to demonstrate the glass protection test (Figure 6E). Briefly, a drop hammer was released from 80 cm height and fell onto a piece of glass laid on with buffer foam or AFSG (Video S3). All the specimens had the same size of 30 × 30 × 5 mm^3. As a control, the glass under bare condition was broken seriously, accompanied by fragments splattering at the impact moment (Figure 6F). After laying on with buffer foams, the drop hammer still easily penetrated protective layers and attacked the glasses, contributing to negligible mitigation in the degree of breakage (Figures 6H–6J). All the failed protection results indicated the impotence of traditional buffer foams in withstanding the high impact energy produced by the hammer. As a comparison, our AFSG exhibited exceptional damage resistance, because the instantaneous structure hardening at the impact area greatly counterbalanced the strike of the hammer (Figure 6G and Video S3).[30] Moreover, derived from the orthogonally laminated structure of AFSG, the synergistic effect of intralayer cracking and interlayer sliding was able to absorb a lot of energy, which further well avoided the breakage of glass.

More drop heights (10–100 cm) were selected to impact the glass. In particular, the conditions protected with AFSG at 20, 40, 60, 80, and 100 cm heights are recorded in Figure S24 and Video S4. AFSG exhibited variable defense capabilities under different drop heights. For 20 cm, elastic deformation along with slight structure hardening of AFSG dominated the role of force dissipation. The higher heights (40–80 cm) further caused growing cracks and interlayer sliding that in turn absorbed substantial impact energy. Even at 100 cm, the whole scaffold fracture as well as extreme impact hardening effectively prevented the glass from being damaged. Force-time curves and corresponding F_{max} during impact process are recorded in Figure S25 and Figure 6K, respectively. Red circles in Figure 6K represent the initial height of glass breakage in terms of specific buffer foam, which suggested that the impact resistance ability improved sequentially from PU to PE to rigid PU. Nonetheless, all results confirmed that AFSG performed the best in force attenuation and maximum buffer time among these protective materials. Taking 80 cm height as an example, the F_{max} of AFSG was only 1.9 kN, less than half that of other foams. It was found that the F_{max} at 100 cm was lower than that at 80 cm. This result was attributed to the whole structure fracture of AFSG, which largely converted the impact energy of the hammer into the kinetic energy of the flying blocks (Video S4). Overall, robust impact resistance allowed the lightweight AFSG to be applied in product transportation and instrument protection as a reasonable alternative to commercial buffer materials.

Generally, thermal attack is another non-negligible threat in extreme environments besides mechanical destruction. Benefiting from oriented hierarchical network and low thermal conductivity (Figure 5E), AFSG exhibited simultaneous thermal protection capacity as verified in the heating demonstration (Figure 6L). Briefly, a heating lamp with 240 W was used to continuously heat an assembled toy man. The body

Please cite this article in press as: Wu et al., A lightweight aramid-based structural composite with ultralow thermal conductivity and high-impact force dissipation, Matter (2022), https://doi.org/10.1016/j.matt.2022.04.031

part was made with polylactic acid with a relatively low melting point of 176°C. It was rapidly melted within 8 min under bare condition accompanied by head drooping (Figure S26A) and collapsed at 18 min (Figure 6M, top). Compared with the severe destruction without any protection (Figure 6N top), the toy man with a 2.5-mm-thick AFSG attached was able to endure heating for up to 60 min (Figure 6M, bottom). Here, only slight deformation was found in the body part (Figure 6N, bottom), and the head drooping at 14 min was due to a3 mild body tilt (Figure S26B). The long-term thermal endurance of AFSG provided feasible protection for equipment/humans in heat-exposed operation.

Flame-retardant performance of F-AFSG

As a major concern in safety management, fire hazards have caused heavy economic loss to society as most modern building facilities face the threat of fire disasters due to their flammability.[37] Herein, to achieve reliable fire protection, a flame-retardant AFSG (F-AFSG, Figure 7A) was further prepared by introducing a small amount of DOPO-HQ (7 phr [parts per hundred rubber]) into SSG. DOPO-HQ (10-(2,5-dihydroxylphenyl)-9,10-dihydro-9-oxa-10-phosphaphenanthrene-10-oxide) is an environment-friendly flame retardant containing a pivotal P-O-C group (inset in Figure S27A), which can be decomposed into phosphorous radicals and eliminate oxygen-containing radicals in gas phase to hinder internal combustion.[38] A thermogravimetric (TG) curve revealed that its T_{max} (temperature at maximum decomposition rate) occurred at 410°C, which represented the scission of the P-O-C bond (Figure S27A).[39] The agglomerated DOPO-HQ nanoparticles (Figure S27B) were homogeneously dispersed in SSG (Figure S28) and then infiltrated into ANF aerogel scaffolds. After orthogonal laminating, the synthetic F-AFSG exhibited a compact laminated structure (Figures 7B, 7C and S29A) with a low density of 0.67 g cm^{-3}. TG analysis reflected an obvious improvement in the thermal stability of F-AFSG (Figure 7D). Compared with AFSG, the early release of phosphorous radicals in DOPO-HQ (T_{max} at 410°C) slowed down the decomposition of SSG, which led to lower T_{max} (456°C) and narrower peak width in the DTG (derivative thermogravimetric) curve of F-AFSG (Figure S29B). The char yield at 800°C also improved significantly, from 11% to 28% (Figure 7D), implying a higher thermal stability of F-AFSG. Furthermore, the addition of DOPO-HQ had a slight influence on the thermal conductivity of F-AFSG (0.098 W m^{-1} k^{-1}; Figure S16), and this value was very similar to that of AFSG (Figure 5E).

A flammability test was carried out to compare the flame-retardant property between F-AFSG and AFSG (corresponding combustion processes are shown in Figures 7E and 7F and Video S5). The ethanol flame rapidly ignited AFSG within 5 s and spread upward to cover the whole block at 10 s. After being subjected to continuous burning for 25 s, AFSG was entirely destroyed under the fire attack, accompanied by the expansion of the white SSG char layer. After the fire source was removed at 26 s, the combustion process of AFSG still continued until the internal SSG was thoroughly carbonized at 82 s (Video S5 and Figure 7G). On the other hand, F-AFSG was burned to a black char layer because of the decomposition of DOPO-HQ (Figure 7H) but not ignited, even though suffering severe combustion for 60 s. The flame also extinguished immediately after the alcohol lamp was removed. The robust fire tolerance as well as the excellent self-extinguishing performance was beneficial in providing valuable rescue time in the fire disasters. Although F-AFSG achieved a salient improvement in flame retardance, excellent mechanical property should be imperative for impact protection. As shown in Figure S30, the compression test confirmed a strong strain rate-dependent behavior of F-AFSG, whose modulus and strength increased significantly, from 1.64 and 0.97 MPa at 0.003 s^{-1} to 3.55 and 1.71 MPa at 0.1 s^{-1}. Clearly, this result indicated that the material was capable of absorbing

Please cite this article in press as: Wu et al., A lightweight aramid-based structural composite with ultralow thermal conductivity and high-impact force dissipation, Matter (2022), https://doi.org/10.1016/j.matt.2022.04.031

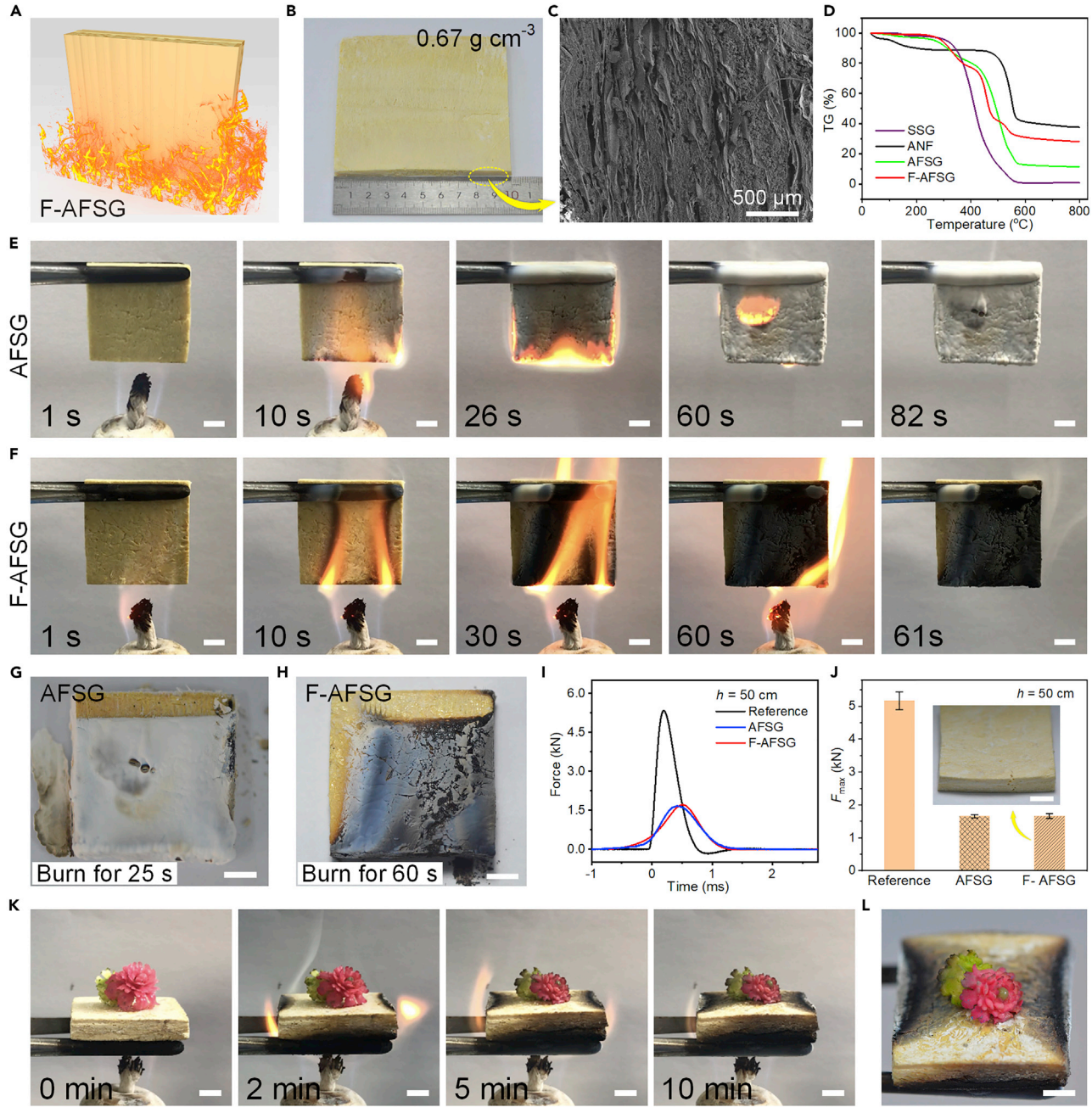

Figure 7. Flame-retardant performance of F-AFSG

(A) Schematic illustrating the flame resistance of F-AFSG.

(B) Optical photograph of F-AFSG with surface area of 10 × 10 cm^2.

(C) Cross-sectional SEM image of F-AFSG.

(D) TG curves of SSG, ANF, AFSG, and F-AFSG.

(E and F) Combustion processes of (E) AFSG and (F) F-AFSG under ethanol flame (see also Video S5). Scale bars, 5 mm.

(G and H) Photographs of (G) AFSG and (H) F-AFSG after burning. Scale bars, 5 mm.

(I) Force-time curves during impact process of AFSG and F-AFSG from 50 cm height.

(J) Comparison of attenuation of F_{max} between AFSG and F-AFSG. Data are represented as mean ± SEM. (Insets represent the surface morphology of F-AFSG after impact. Scale bar, 5 mm).

(K) Combustion process showing the excellent fire-proofing property of F-AFSG (see also Video S6). Scale bars, 5 mm.

(L) Final appearance of flowers after burning for 10 min. Scale bar, 5 mm.

Please cite this article in press as: Wu et al., A lightweight aramid-based structural composite with ultralow thermal conductivity and high-impact force dissipation, Matter (2022), https://doi.org/10.1016/j.matt.2022.04.031

massive energy at high strain rate. Furthermore, the hammer-dropping test at 10–70 cm height was implemented to evaluate the dynamic force buffering the effect of F-AFSG. At 50 cm height, the recorded force-time curve showed an almost consistent impact course with AFSG (Figure 7I) while maintaining high attenuation of F_{max} (67%; Figure 7J). Other impact heights also showed prominent impact dissipation (53%–76%; Figure S31), demonstrating that DOPO-HQ showed a slight influence on the anti-impact capacity of F-AFSG.

In short, the lightweight flame retardant AFSG exhibited robust fire endurance (at least 60 s) and rapid self-extinguishing, as well as high force dissipation, which was promising in the simultaneous demand for impact protection and firefighting. As shown in Figure 7K and Video S6, an ultralong flame insulation process verified its practicability in fire safety. The laminated structure of F-AFSG effectively suppressed the fire spread and heat transfer generated by the fire source and further avoided the catastrophic destruction of the flowers. After combustion for 10 min, the flowers just shrank due to surrounding heat diffusion while their initial luster and morphology were maintained (Figure 7L), which demonstrated the reliable protection of F-AFSG in fire hazard.

Conclusions

In summary, a lightweight (0.46 g cm^{-3}) structural composite (AFSG) with ultralow thermal conductivity (0.09 W m^{-1} k^{-1}) and high-impact force dissipation (65% attenuation for 6.34 kN) was proposed through orthogonally laminating the SSG-infiltrated porous ANF aerogel networks. By virtue of the unique voids-SSG coexistence structure, AFSG possessed a perfect reconciliation between thermal resistance and impact energy absorption that outperformed most existing cushioning materials such as natural rubber and PDMS. Microsize voids that were randomly distributed in AFSG greatly eliminated air convection and weakened heat conduction along the direction of lamination, thus enabling a wide insulation range (−120 to 300°C) as well as long-term thermal resistance capacity (300°C for 30 min). In addition, derived from dynamic force impedance of B-O crosslinks and internal friction among entangled SSG molecular chains, AFSG exhibited a significant stress enhancement effect under high strain rate loading and performed exceptional force dissipation toward drop hammer striking. Furthermore, the failure mechanism of intralayer crack accompanying interlayer sliding assisted AFSG in absorbing excessive mechanical energy and provided better protection to brittle glass than commercial buffer foams against impact damage. Moreover, by introducing a small amount of flame retardant, AFSG could acquire robust fire endurance (rapidly self-extinguishing after burning for 60 s) without sacrificing the original force attenuation behavior. Overall, the lightweight AFSG showed broad potential in simultaneously impacting dissipation and thermal protection as an ideal candidate for next-generation multifunctional protective materials.

EXPERIMENTAL PROCEDURES

Resource availability

Lead contact

Further information and requests for resources should be directed to and will be fulfilled by the lead contact, Prof. Xinglong Gong (gongxl@ustc.edu.cn).

Materials availability

This study did not generate new unique reagents.

Data and code availability

This study did not generate or analyze datasets or code.

Please cite this article in press as: Wu et al., A lightweight aramid-based structural composite with ultralow thermal conductivity and high-impact force dissipation, Matter (2022), https://doi.org/10.1016/j.matt.2022.04.031

Materials

Aramid fabrics were obtained from Junantai Co. Potassium hydroxide (KOH), dimethyl sulfoxide (DMSO), boric acid, and hydroxyl silicone oil were purchased from Sinopharm Chemical Reagent Co. Fire retardant 10-(2,5-dihydroxyphenyl)-10-hydro-9-oxa-10-phosphaphenanthrene-10-oxide (DOPO-HQ), was supplied by Changzhou Zhuolian Zhichuang Polymer Material Co.

Preparation of aramid nanofiber aerogel

Aramid fabrics (7.5 g) and KOH (7.5 g) were dissolved in DMSO (535 g) to obtain ANF-DMSO dispersion according to early report.[40] The ANF-DMSO dispersion was further immersed in deionized water to form ANF hydrogel with specific size. After residual DMSO being rinsed by deionized water, the ANF hydrogel was placed on a copper plate surface (−70°C) in contact with liquid nitrogen for unidirectional freezing (Figure S1). The frozen ANF hydrogel was then subjected to freeze-drying at −50°C and 10 Pa for 48 h to obtain ANF aerogel.

Preparation of shear stiffening gel

The preparation process of SSG could be found in our previous report.[41] Briefly, boric acid and hydroxyl silicone oil (mass ratio, 1:20) were mixed and stirred at 160°C for 2 h. After full reaction, viscoelastic SSG was formed with abundant boron-oxygen crosslinking bonds. The prepared SSG was then mixed with ethanol (mass ratio, 2:1) to obtain homogeneous SSG/ethanol dispersion. A comparison of rheology property between original SSG and SSG after eliminating ethanol was shown in Figure S35. The variation of storage modulus to frequency reflected a slight degradation in shear stiffening performance after removal of ethanol. The appearance was also consistent to original SSG (inset of Figure S35). Therefore, ethanol was chosen as a solvent to disperse SSG.

Preparation of ANF@SSG composite AFSG and fire-retardant AFSG (F-AFSG)

First, ANF aerogel was completely soaked in SSG-ethanol dispersion and ultrasonicated for sufficient infiltration. Then, a pair of ANF aerogels with the same size were taken out and laminated orthogonally, followed by hot-pressing toward the lamination direction at 80°C for 24 h. To acquire excellent thermal insulation and anti-impact performances, the compression strain was controlled at about 80% (see Note S3). Note that the laminated direction was perpendicular to the freezing direction (Figure 1A). After the ethanol evaporated thoroughly from the SSG, AFSG with densified laminated structure was obtained. For comparison, a pair of original ANF aerogels were laminated orthogonally and hot-pressed directly to prepare the densified ANF block.

Similarly to AFSG, F-AFSG was also fabricated by soaking, laminating, and hot-pressing treatments. Before lamination, ANF aerogel was soaked in the aforementioned SSG-ethanol dispersion added to fire retardant DOPO-HQ, where the mass ratio of SSG to DOPO-HQ was 100:7.

Characterization and test

Morphologies of ANF aerogel and SSG were observed by scanning electron microscopy (SEM; Gemini 500, Carl Zeiss Jena, Germany). Chemical functional groups of AFSG were identified on a Fourier transform infrared spectrometer (FTIR Nicolet 8700; Thermo Nicolet, USA). Thermal stability of AFSG was performed on a thermogravimetric analyzer (TGA Q5000IR, TA, USA) heating from 30 to 800°C by 10°C min^{-1} in a nitrogen environment. The rheological and creep behaviors of SSG (Φ20 mm × 1 mm) were tested on a rheometer (Physica MCR 302, Anton Paar, Austria) using a parallel plate (PP20) under 25°C. A universal tensile instrument (MTS Criterion model 43) was employed to test the low strain rate compressive properties of AFSG (10 × 10 × 10 mm^3). High strain

rate compression test was conducted on a spilt Hopkinson pressure bar (SHPB) device, which consisted of bullet, incident bar, transmission bar, and absorber bar. The velocity of bullet was captured by photoelectric gate. All specimens had a diameter of 14 mm and a thickness of 2.4 mm. In all compression tests, the compressive direction was perpendicular to the freezing direction. A drop tower equipment (ZCJ1302-A, MTS, USA) was employed for impact resistance testing, where a rod-like hammer weighting 0.55 kg was released from specified height to freely impact on specimens placed on the surface of force sensor (Figure 4A). The dimensions of the specimens were 25 × 25 × 5 mm^3. Force and acceleration signals during e thimpact process were acquired by force sensor and accelerometer. Thermal conductivity of AFSG perpendicular to freezing direction was determined by a laser thermal conductivity meter (LFA457, NETZSCH, Germany). A flammability test was carried out to evaluate the fire endurance of F-AFSG with a size of 25 × 25 × 5 mm^3 using an alcohol lamp. The burning direction was parallel to the freezing direction.

Impact simulation

Dynamic impact process of AFSG was simulated using finite element method by Abaqus/Explicit. The representative voids-SSG coexistence structure of AFSG consisted of cellular ANF walls and filled SSG (Figure S12B), in which ANF walls and SSG were constructed by hollow and solid elements, respectively. According to our previous report,[41] a standard linear solid (SLS) model was used to describe the rate-dependent mechanical behavior of SSG (see Note S1). The micromodel of AFSG had an area of about 0.9 × 0.4 mm^2 and a height of about 0.5 mm, which was compressed by a rigid plate (23 mg) with an initial velocity of 0.4 m s^{-1}. The contact force at each time step between AFSG and ground was extracted.

SUPPLEMENTAL INFORMATION

Supplemental information can be found online at https://doi.org/10.1016/j.matt.2022.04.031.

ACKNOWLEDGMENTS

Financial support from the National Natural Science Foundation of China (grant nos. 12132016, 11972032, 11972337, and 12072338), the Aviation Science Foundation of China (20200029079004), and the Fundamental Research Funds for the Central Universities (WK2480000007) are gratefully acknowledged. The study is also supported by USTC Center for Micro- and Nanoscale Research.

AUTHOR CONTRIBUTIONS

S.X. and X.G. designed and supervised the whole project. J.Z., Z.F., Q.S., X.H., and J.W. fabricated and characterized the composites, designed and completed the experiments, and analyzed the data. C.Z. and Y.W. simulated the mechanical impact process. J.W. and S.X. wrote the manuscript. All the authors were actively involved in discussion, analysis, and revision.

DECLARATION OF INTERESTS

The authors declare no competing interests.

Received: December 8, 2021
Revised: March 7, 2022
Accepted: April 26, 2022
Published: May 17, 2022

REFERENCES

1. Xu, L.F., Meng, X.W., and Xu, X.G. (2014). Natural hazard chain research in China: a review. Nat. Hazards *70*, 1631–1659. https://doi.org/10.1007/s11069-013-0881-x.

2. Garlock, M., Paya-Zaforteza, I., Kodur, V., and Gu, L. (2012). Fire hazard in bridges: review, assessment and repair strategies. Eng. Struct. *35*, 89–98. https://doi.org/10.1016/j.engstruct.2011.11.002.

3. Dong, S.N., Wang, H., Guo, X.M., and Zhou, Z.F. (2021). Characteristics of water hazards in China's coal mines: a review. Mine Water Environ. *40*, 325–333. https://doi.org/10.1007/s10230-021-00770-6.

4. Hazarika, A., Deka, B.K., Kim, D., Jeong, H.E., Park, Y.B., and Park, H.W. (2018). Woven Kevlar fiber/polydimethylsiloxane/reduced graphene oxide composite-based personal thermal management with freestanding Cu-Ni core-shell nanowires. Nano Lett. *18*, 6731–6739. https://doi.org/10.1021/acs.nanolett.8b02408.

5. Yuan, F., Liu, S., Zhou, J.Y., Fan, X.W., Wang, S., and Gong, X.L. (2020). A smart Kevlar-based triboelectric nanogenerator with enhanced anti-impact and self-powered sensing properties. Smart Mater. Struct. *29*, 125007. https://doi.org/10.1088/1361-665X/abaf08.

6. Sang, M., Wu, Y.X., Liu, S., Bai, L.F., Wang, S., Jiang, W.Q., Gong, X.L., and Xuan, S.H. (2021). Flexible and lightweight melamine sponge/Mxene/polyborosiloxane (MSMP) hybrid structure for high-performance electromagnetic interference shielding and anti-impact safe-guarding. Compos. Part B-Eng. *211*, 108669. https://doi.org/10.1016/j.compositesb.2021.108669.

7. Zhou, J.Y., Zhang, J.S., Sang, M., Liu, S., Yuan, F., Wang, S., Sun, S.S., and Gong, X.L. (2022). Advanced functional Kevlar composite with excellent mechanical properties for thermal management and intelligent safeguarding. Chem. Eng. J. *428*, 131878. https://doi.org/10.1016/j.cej.2021.131878.

8. Ha, N.S., and Lu, G.X. (2020). A review of recent research on bio-inspired structures and materials for energy absorption applications. Compos. Part B-Eng. *181*, 107496. https://doi.org/10.1016/j.compositesb.2019.107496.

9. Zhao, N.F., Li, M., Gong, H.X., and Bai, H. (2020). Controlling ice formation on gradient wettability surface for high-performance bioinspired materials. Sci. Adv. *6*, eabb4712. https://doi.org/10.1126/sciadv.abb4712.

10. Behera, R.P., and Le Ferrand, H. (2021). Impact-resistant materials inspired by the mantis shrimp's dactyl club. Matter *4*, 2831–2849. https://doi.org/10.1016/j.matt.2021.07.012.

11. Quan, H.C., Yang, W., Schaible, E., Ritchie, R.O., and Meyers, M.A. (2018). Novel defense mechanisms in the armor of the scales of the "living fossil" coelacanth fish. Adv. Funct. Mater. *28*, 1804237. https://doi.org/10.1002/adfm.201804237.

12. Zhan, H.J., Wu, K.J., Hu, Y.L., Liu, J.W., Li, H., Guo, X., Xu, J., Yang, Y., Yu, Z.L., Gao, H.L., et al. (2019). Biomimetic carbon tube aerogel enables super-elasticity and thermal insulation. Chem *5*, 1871–1882. https://doi.org/10.1016/j.chempr.2019.04.025.

13. Xu, X., Zhang, Q.Q., Hao, M.L., Hu, Y., Lin, Z.Y., Peng, L.L., Wang, T., Ren, X.X., Wang, C., Zhao, Z.P., et al. (2019). Double-negative-index ceramic aerogels for thermal superinsulation. Science *363*, 723–727. https://doi.org/10.1126/science.aav7304.

14. Zhao, S.Y., Malfait, W.J., Guerrero-Alburquerque, N., Koebel, M.M., and Nystrom, G. (2018). Biopolymer aerogels and foams: chemistry, properties, and applications. Angew. Chem. Int. Ed. *57*, 7580–7608. https://doi.org/10.1002/anie.201709014.

15. Mao, A.R., Zhao, N.F., Liang, Y.H., and Bai, H. (2021). Mechanically efficient cellular materials inspired by cuttlebone. Adv. Mater. *33*, 2007348. https://doi.org/10.1002/adma.202007348.

16. Rostami, J., Gordeyeva, K., Benselfelt, T., Lahchaichi, E., Hall, S.A., Riazanova, A.V., Larsson, P.A., Cinar Ciftci, G., and Wagberg, L. (2021). Hierarchical build-up of bio-based nanofibrous materials with tunable metal-organic framework biofunctionality. Mater. Today *48*, 47–58. https://doi.org/10.1016/j.mattod.2021.04.013.

17. Zou, S.B., Therriault, D., and Gosselin, F.P. (2020). Spiderweb-inspired, transparent, impact-absorbing composite. Cell Rep. Phys. Sci. *1*, 100240. https://doi.org/10.1016/j.xcrp.2020.100240.

18. Cao, X.Q., Vassen, R., and Stoever, D. (2004). Ceramic materials for thermal barrier coatings. J. Eur. Ceram. Soc. *24*, 1–10. https://doi.org/10.1016/S0955-2219(03)00129-8.

19. Gonzalez, G.M., Ward, J., Song, J., Swana, K., Fossey, S.A., Palmer, J.L., Zhang, F.W., Lucian, V.M., Cera, L., Zimmerman, J.F., et al. (2020). para-aramid fiber sheets for simultaneous mechanical and thermal protection in extreme environments. Matter *3*, 742–758. https://doi.org/10.1016/j.matt.2020.06.001.

20. Liu, Z.W., Lyu, J., Fang, D., and Zhang, X.T. (2019). Nanofibrous Kevlar aerogel threads for thermal insulation in harsh environments. ACS Nano *13*, 5703–5711. https://doi.org/10.1021/acsnano.9b01094.

21. Yin, Z., Hannard, F., and Barthelat, F. (2019). Impact-resistant nacre-like transparent materials. Science *364*, 1260–1263. https://doi.org/10.1126/science.aaw8988.

22. Huang, C.J., Peng, J.S., Wan, S.J., Du, Y., Dou, S.X., Wagner, H.D., Tomsia, A.P., Jiang, L., and Cheng, Q.F. (2019). Ultra-tough inverse artificial nacre based on epoxy-graphene by freeze-casting. Angew. Chem. Int. Ed. *58*, 7636–7640. https://doi.org/10.1002/anie.201902410.

23. Song, J.W., Chen, C.J., Zhu, S.Z., Zhu, M.W., Dai, J.Q., Ray, U., Li, Y.J., Kuang, Y.D., Li, Y.F., Quispe, N., et al. (2018). Processing bulk natural wood into a high-performance structural material. Nature *554*, 224–228. https://doi.org/10.1038/nature25476.

24. Eom, W., Lee, S.H., Shin, H., Jeong, W., Koh, K.H., and Han, T.H. (2021). Microstructure-controlled polyacrylonitrile/graphene fibers over 1 gigapascal strength. ACS Nano *15*, 13055–13064. https://doi.org/10.1021/acsnano.1c02155.

25. Li, X., Dong, G.Q., Liu, Z.W., and Zhang, X.T. (2021). Polyimide aerogel fibers with superior flame resistance, strength, hydrophobicity, and flexibility made via a universal sol-gel confined transition strategy. ACS Nano *15*, 4759–4768. https://doi.org/10.1021/acsnano.0c09391.

26. Fears, T.M., Hammons, J.A., Sain, J.D., Nielsen, M.H., Braun, T., and Kucheyev, S.O. (2018). Ultra-low-density silver aerogels via freeze-substitution. APL Mater. *6*, 091103. https://doi.org/10.1063/1.5039521.

27. Wang, M.Q., Vecchio, D., Wang, C.Y., Emre, A., Xiao, X.Y., Jiang, Z.X., Bogdan, P., Huang, Y.D., and Kotov, N.A. (2020). Biomorphic structural batteries for robotics. Sci. Robot. *5*, eaba1912. https://doi.org/10.1126/scirobotics.aba1912.

28. Ma, Z.L., Kang, S.L., Ma, J.Z., Shao, L., Wei, A.J., Liang, C.B., Gu, J.W., Yang, B., Dong, D.D., Wei, L.F., and Ji, Z. (2019). High-performance and rapid-response electrical heaters based on ultraflexible, heat-resistant, and mechanically strong aramid nanofiber/Ag nanowire nanocomposite papers. ACS Nano *13*, 7578–7590. https://doi.org/10.1021/acsnano.9b00434.

29. Xie, C.J., He, L.Y., Shi, Y.F., Guo, Z.X., Qiu, T., and Tuo, X.L. (2019). From monomers to a lasagna-like aerogel monolith: an assembling strategy for aramid nanofibers. ACS Nano *13*, 7811–7824. https://doi.org/10.1021/acsnano.9b01955.

30. Zhao, C.Y., Gong, X.L., Wang, S., Jiang, W.Q., and Xuan, S.H. (2020). Shear stiffening gels for intelligent anti-impact applications. Cell Rep. Phys. Sci. *1*, 100266. https://doi.org/10.1016/j.xcrp.2020.100266.

31. Ferraro, C., Garcia-Tunon, E., Rocha, V.G., Barg, S., Farinas, M.D., Alvarez-Arenas, T.E.G., Sernicola, G., Giuliani, F., and Saiz, E. (2016). Light and strong SiC networks. Adv. Funct. Mater. *26*, 1636–1645. https://doi.org/10.1002/adfm.201504051.

32. Su, L., Wang, H.J., Niu, M., Dai, S., Cai, Z.X., Yang, B.G., Huyan, H.X., and Pan, X.Q. (2020). Anisotropic and hierarchical SiC@SiO_2 nanowire aerogel with exceptional stiffness and stability for thermal superinsulation. Sci. Adv. *6*, eaay6689. https://doi.org/10.1126/sciadv.aay6689.

33. Zhang, S.S., Wang, S., Wang, Y.P., Fan, X.W., Ding, L., Xuan, S.H., and Gong, X.L. (2018). Conductive shear thickening gel/polyurethane sponge: a flexible human motion detection sensor with excellent safeguarding performance. Compos. Part. A-Appl. S. *112*, 197–206. https://doi.org/10.1016/j.compositesa.2018.06.007.

34. Zhu, J., Yang, M., Emre, A., Bahng, J.H., Xu, L.Z., Yeom, J., Yeom, B., Kim, Y., Johnson, K., Green, P., and Kotov, N.A. (2017). Branched aramid nanofibers. Angew. Chem. Int. Ed. *56*, 11744–11748. https://doi.org/10.1002/anie.201703766.

35. Aleman, B., Reguero, V., Mas, B., and Vilatela, J.J. (2015). Strong carbon nanotube fibers by drawing inspiration from polymer fiber spinning. ACS Nano *9*, 7392–7398. https://doi.org/10.1021/acsnano.5b02408.

36. Benedetti, M., du Plessis, A., Ritchie, R.O., Dallago, M., Razavi, S.M.J., and Berto, F. (2021). Architected cellular materials: a review on their mechanical properties towards fatigue-tolerant design and fabrication. Mat. Sci. Eng. R. *144*, 100606. https://doi.org/10.1016/j.mser.2021.100606.

37. Lazar, S.T., Kolibaba, T.J., and Grunlan, J.C. (2020). Flame-retardant surface treatments. Nat. Rev. Mater. *5*, 259–275. https://doi.org/10.1038/s41578-019-0164-6.

38. Shi, X.X., Peng, X.F., Zhu, J.Y., Lin, G.Y., and Kuang, T.R. (2018). Synthesis of DOPO-HQ-functionalized graphene oxide as a novel and efficient flame retardant and its application on polylactic acid: thermal property, flame retardancy, and mechanical performance. J. Colloid Interf. Sci. *524*, 267–278. https://doi.org/10.1016/j.jcis.2018.04.016.

39. He, M., Zhang, D.H., Zhao, W., Qin, S.H., and Yu, J. (2019). Flame retardant and thermal decomposition mechanism of poly(butylene terephthalate)/DOPO-HQ composites. Polym. Compos. *40*, 974–985. https://doi.org/10.1002/pc.24772.

40. Yang, M., Cao, K.Q., Sui, L., Qi, Y., Zhu, J., Waas, A., Arruda, E.M., Kieffer, J., Thouless, M.D., and Kotov, N.A. (2011). Dispersions of aramid nanofibers: a new nanoscale building block. ACS Nano *5*, 6945–6954. https://doi.org/10.1021/nn2014003.

41. Zhao, C.Y., Wang, Y., Ni, M.Y., He, X.K., Xuan, S.H., and Gong, X.L. (2021). Dynamic behavior of impact hardening elastomer: a flexible projectile material with unique rate-dependent performance. Compos. Part. A-Appl. S. *143*, 106285. https://doi.org/10.1016/j.compositesa.2021.106285.